


RESEARCH ARTICLE **OPEN ACCESS**

Electrochemical Modeling and Degradation Analysis of Lithium-Ion Batteries in High Temperature Environments

Fei Chen¹ | Fan Yang¹ | Haoran Chu² | Jiatong Xu¹ | Kaiyi Yang¹ | Justice D. Akoto³ | Ali Haider⁴ | Xingrui Wang¹ | Jie Yang⁵ | Xinhua Liu^{1,6} | Zhiming Feng⁷  | Rui Tan³

¹School of Transportation Science and Engineering, Beihang University, Beijing, China | ²School of Electronic and Information Engineering, Beihang University, Beijing, China | ³Department of Chemical Engineering, Swansea University, Swansea, UK | ⁴Department of chemistry, Quaid-i-Azam University, Islamabad, Pakistan | ⁵Energy Innovation Centre, Warwick Manufacturing Group, University of Warwick, Coventry, UK | ⁶Dyson School of Design Engineering, Imperial College London, South Kensington Campus, London, UK | ⁷Department of Chemical Engineering, The University of Manchester, Manchester, UK

Correspondence: Xinhua Liu (liuxinhua19@buaa.edu.cn) | Zhiming Feng (zhiming.feng@manchester.ac.uk)

Received: 8 June 2025 | **Revised:** 19 September 2025 | **Accepted:** 28 September 2025

Funding: This study was supported by National Natural Science Foundation of China (No. 52102470) (No. 52302486) and National Key Research and Development Program of China (No. 2021YFB2501300).

Keywords: aging mechanisms | electrochemical-mechanical coupling | life prediction | lithium-ion battery | solid electrolyte interphase growth

ABSTRACT

Simulation models are of great importance in understanding the complexities of the internal electrochemical processes within batteries, aiding in design optimization and advancing energy storage technologies. One of the central challenges lies in predicting battery lifespan and elucidating side reactions under extreme operating conditions. This study aims to design an electrochemical model that considers multiple side reactions to predict the cycle life of lithium-ion batteries in high temperature environments. First, a basic simulation framework is established using a simplified electrochemical-mechanical coupling model. Subsequently, multiscale characterization of aged batteries is performed to identify five types of side reactions, encompassing phenomena such as solid electrolyte interphase (SEI) growth, cracking of negative electrode particles, electrolyte oxidation and decomposition/deposition of active materials. A comprehensive battery life prediction model is constructed by modeling these side reactions. Finally, the accuracy of the life prediction is validated using high temperature cycling data. The conclusions reveal that electrolyte decomposition and the loss of active material are the primary causes of battery degradation under high temperature conditions.

1 | Introduction

Achieving net-zero emissions and climate neutrality has placed increasing emphasis on the development and deployment of low-carbon technologies across energy systems [1–6]. Among these, CO₂ reduction and capture strategies, along with other emerging low-carbon approaches, are receiving growing attention for their potential to directly mitigate greenhouse gas

emissions [7–10]. In parallel, the widespread integration of renewable energy sources, including solar, wind, and hydrogen, presents new challenges for energy management, particularly due to the variability and intermittency of power generation [11–17]. These challenges highlight the growing need for efficient and dependable energy storage systems to ensure stable and resilient grid operation [18–21]. Among various storage technologies, lithium-ion batteries (LIBs) are widely adopted

This is an open access article under the terms of the [Creative Commons Attribution](https://creativecommons.org/licenses/by/4.0/) License, which permits use, distribution and reproduction in any medium, provided the original work is properly cited.

© 2025 The Author(s). *Battery Energy* published by Xijing University and John Wiley & Sons Australia, Ltd.

due to their high energy density, long operational lifespan, and favorable electrochemical performance [22–25]. Nonetheless, LIBs are subject to gradual degradation during extended use, especially under elevated temperature or high-rate cycling conditions, which can lead to capacity loss, shortened service life, and increased safety risks [26–29]. Improving the durability of LIBs is therefore critical for supporting the long-term performance and economic feasibility of energy storage in low-carbon and renewable energy infrastructures [30, 31]. To optimize their performance across diverse climatic conditions and enable reliable health monitoring, a systematic investigation of the complex interactions between multiple degradation mechanisms is essential [32–36]. In particular, elevated temperature has been recognized as a major factor accelerating degradation, yet the predictive modeling of such thermally-driven aging processes remains insufficiently explored.

The degradation of LIBs stems from complex, interrelated aging mechanisms that evolve over time. The direct observation of internal chemical reactions remains inherently challenging, particularly in capturing the dynamics of side reactions under extreme operational conditions, where multiple degradation pathways interact synergistically [37–39]. To address these complexities, recent studies have employed advanced modeling and computational techniques [40]. For instance, Lee et al. developed an electrochemical-mechanical phase field model to simulate the growth of dendrites on the actual electrode surface morphology [41]. The findings elucidate that the electric field concentrated at the dendrite tips serves as the principal driving force for lithium ion transport and the induction of dendrite growth. Complementing this, Sun et al. [42] used *ab initio* molecular dynamics (AIMD) to demonstrate that ethylene carbonate (EC) solvent decomposition is the primary origin of solid-electrolyte interphase (SEI) formation. Meanwhile, Zhang et al. investigated the latest developments in comprehending oxygen loss and structural degradation in layered oxide cathodes [43]. They provided a thorough analysis of the complex reaction mechanisms linked to oxygen loss-induced structural degradation. While extensive research has advanced the understanding of battery degradation mechanisms through detailed microscale analyses, a critical knowledge gap persists in establishing robust correlations between these internal aging processes and the resultant macroscopic performance deterioration such as capacity loss and lifespan. Current investigations have yet to bridge this divide, limiting our ability to predict long-term battery behavior and develop targeted mitigation strategies.

The longevity or state of health (SOH) of a battery reflects its current ability to store and deliver energy compared with its initial condition. Accurate SOH prediction is critical for ensuring safe energy storage system operation and preventing thermal/electrical failures. Various modeling approaches have emerged for capacity degradation forecasting and SOH estimation, including equivalent circuit models (ECMs), empirical models, electrochemical models, and machine learning techniques [44]. The ECM method treats the parameters of the equivalent circuit components as state variables. By employing data fusion techniques such as Kalman filtering, particle filtering, and Unscented Kalman filtering, the method optimizes estimation results based on the deviations between predicted and actual values [45–47]. Empirical models for capacity

degradation estimation typically fit known data using polynomial or exponential functions or through parameter identification [48–51]. These models often depend on the parameter identification process, which limits their generalization capabilities and makes them sensitive to environmental factors, potentially leading to significant errors. In contrast, machine learning models have gained widespread attention due to their improved versatility and accuracy in state estimation [52–54]. These algorithms are effective tools for function approximation, as they can unveil latent mapping relationships between data points, thereby eliminating the necessity for intricate physical modeling procedures [55]. However, machine learning models struggle to handle challenges in out-of-distribution (OOD) generalization, requiring substantial experimental data for training model parameters and incurring considerable computational expenses during parameter optimization. These challenges highlight the limitations of existing data-driven and equivalent-circuit-based approaches in physically interpreting capacity fade under varying thermal conditions. A modeling approach that explicitly considers internal physicochemical mechanisms while maintaining reasonable computational cost is therefore essential for high-temperature reliability analysis.

In comparison to the methods mentioned above, electrochemical modeling approaches offer distinct advantages by enabling comprehensive analysis of battery degradation mechanisms while capturing intricate internal reaction dynamics without requiring extensive historical training data. For example, Yu et al. developed a model for calculating battery life cycle capacity degradation, utilizing a simplified electrochemical model and the kinetic Monte Carlo (kMC) method [56]. The electrochemical model provides real-time internal state variables for kMC calculations, while the kMC model analyzes the growth of SEI films from a microscopic perspective, focusing on the evolution of molecules. Similarly, Gao et al. demonstrated the effectiveness of combining a full-order Pseudo-Two-Dimensional (P2D) model with dual extended Kalman filters for simultaneous estimation of state of charge (SOC) and SOH. The model considered SEI growth as the main factor of degradation and expressed accurate voltage response across several operating conditions [57]. Currently, most battery modeling techniques are based on the P2D model, which couples several differential equations to describe lithium diffusion in electrodes, redox reactions at the electrode/electrolyte interface, and lithium-ion diffusion in the electrolyte. The P2D modeling framework systematically integrates fundamental physicochemical principles to describe battery behavior across multiple scales. At its core, the model employs: (i) Ohm's law for electric potential distribution, (ii) Fick's law of diffusion for ion transport dynamics, (iii) the Butler-Volmer equation to quantify electrode reaction kinetics as a function of overpotential, and (iv) the Nernst equation relating equilibrium potential to local reaction conditions. This multi-physics approach not only captures the three primary operational processes (charge transport, mass transport, and interfacial reactions) but also model side-reaction, thereby enabling the accurate capture of processes such as battery aging, heat generation, gas generation, and thermal runaway. However, despite the strength of the P2D framework, most existing models still simplify degradation behavior by isolating single mechanisms, limiting their ability to reproduce the coupled aging effects observed under long-term high-temperature cycling.

Temperature represents a critical, yet understudied factor in battery safety and performance. While thermal effects significantly influence battery behavior, current research exhibits three key limitations: (1) insufficient investigation of internal state evolution under elevated temperatures, (2) inadequate simulation of thermally accelerated side reactions, and (3) limited predictive capability for high-temperature aging scenarios. Furthermore, existing electrochemical models frequently oversimplify degradation processes by focusing on isolated aging mechanisms rather than their synergistic interactions [58, 59]. To enhance the accuracy of capacity degradation prediction for individual batteries under high temperature conditions, we develop a multi side reaction coupled model for battery life prediction. By examining the effects and processes of five aging modes on battery life, including SEI growth, fragmentation of negative electrode particles, electrolyte oxidation, and decomposition/deposition of active materials, the coupling relationships between multiple aging factors are identified. In this work, a degradation modeling framework is established by coupling multiple reaction mechanisms, including SEI growth, particle fracture in the negative electrode, electrolyte oxidation, LiPF_6 decomposition, and Mn dissolution. The applicability of the proposed framework at elevated temperature arises from the inclusion of these fundamental degradation mechanisms, which are significantly accelerated at 60°C and thus become dominant. By explicitly representing these processes, the framework successfully reproduces the observed capacity fade trends during long-term cycling and is validated by post-mortem characterization (SEM, XPS, XRD, Raman). The framework therefore provides new insights into degradation behavior under elevated-temperature conditions and offers practical value for assessing battery reliability in high-temperature applications. By bridging the gap between theoretical modeling and real-world degradation behaviors at high temperatures of LIBs, this study will potentially contribute to more reliable lifetime estimation, especially at high temperatures, improved fast-charging protocols and safer battery design. The present model emphasizes the interactive behavior among multiple aging mechanisms under continuous high-temperature cycling. A simulation framework is constructed to resolve the temporal and spatial evolution of degradation-driven variables and their influence on capacity fade. Model predictions are systematically

compared with electrochemical performance and validated through post-mortem observations, including structural, morphological, and compositional changes. This combined modeling and experimental strategy enables a more robust understanding of failure modes under thermal stress and supports improved predictive capability in battery life assessment.

2 | Methodology

2.1 | Electrochemical Model

The objective of this study is to develop a physics-based electrochemical model that will facilitate a more profound understanding of the electrochemical dynamics under high temperature conditions. Although ambient temperatures exceeding 60°C are rare, this study simulates operating environments typical of battery packs in electric vehicles and grid-scale storage systems exposed to external heat, insufficient cooling, or thermal runaway precursors. For instance, under direct sunlight or in under-hood EV placements, local battery temperatures can surpass 60°C , even if ambient conditions are lower [60–62]. Moreover, international safety standards such as IEC 62660-2 recommend thermal abuse testing at elevated temperatures to evaluate worst-case scenarios [63]. As illustrated in Figure 1, the established electrochemical model comprises five main elements: anode current collector, negative electrode, separator, positive electrode, and cathode current collector. The cathode material used in the experiment is NCM523, with the chemical formula $\text{LiNi}_{0.5}\text{Co}_{0.2}\text{Mn}_{0.3}\text{O}_2$. This material possesses a layered rock-salt structure of the $\alpha\text{-NaFeO}_2$ type, belonging to the R-3m space group. The anode material is graphite. The material parameters required for modeling are referenced from the literature [64]. The model is based on the P2D model, where the transport behavior of lithium ions is only considered in the thickness direction. The solid phase of the porous electrode is defined as spherical particles, with the electrolyte filling the entire space. Therefore, another “pseudo” dimension, denoted as the radial dimension r through the thickness of each spherical electrode particle, is also considered in the electrode domain [65]. In this study, an electrochemical model was constructed using COMSOL Multiphysics.

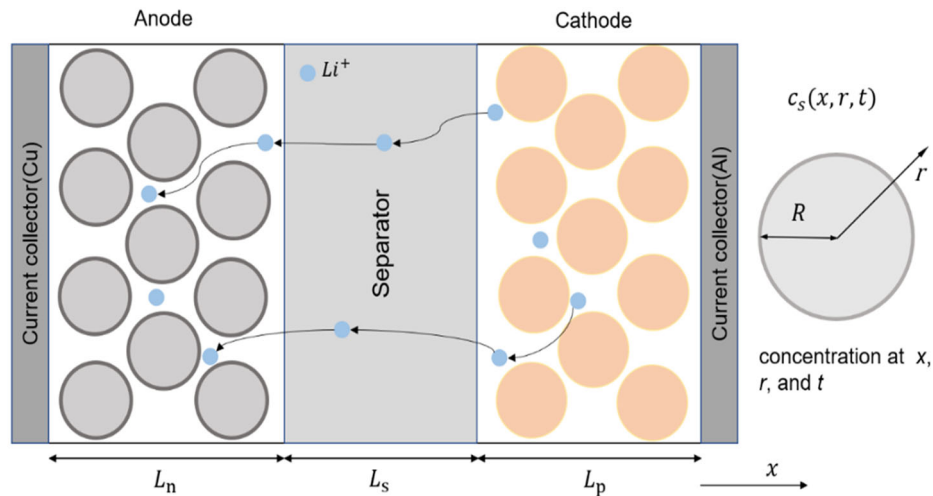


FIGURE 1 | Schematic diagram of the P2D model.

The decomposition/deposition model of Mn was built using the dilute matter transfer module.

The fundamental equations of the model, which encompass conservation of mass, conservation of charge and kinetic model are presented in Table 1.

2.2 | Electrochemical-Mechanical Couple Model

The stress resulting from the diffusion of Li is intimately associated with the distribution of lithium-ion concentration. The computation of stress and strain fields induced by lithium-ion diffusion is enabled by the treatment of the active material as isotropic ideal spheres. Under the assumption that that spherical particles are considered to be linear elastic solids that are not affected by external forces, their elastic characteristics remain unaffected by the lithium concentration. The correlation between stress and strain during lithium-ion diffusion is illustrated as follows:

$$\varepsilon_{ij} = \frac{1}{E} [(1 + \nu)\sigma_{ij} - \nu\sigma_{ij}\delta_{ij}] + \frac{\Delta c_s \Omega}{3} \delta_{ij} \quad (7)$$

where ε_{ij} is the strain tensor, σ_{ij} is the stress tensor (Pa), δ_{ij} is the Kronecker delta, E is the Young's modulus (Pa), ν is the Poisson's ratio, Δc_s is the change of lithium concentration in the solid phase ($\text{mol}\cdot\text{m}^{-3}$), and Ω is the partial molar volume of lithium in the active material ($\text{m}^3\cdot\text{mol}^{-1}$).

In a spherical coordinate system, the aforementioned Equation (7) can be decomposed into the stress-strain relationships along the radial and tangential directions within the electrode:

$$\begin{cases} \varepsilon_r = \frac{1}{E}(\sigma_r - 2\nu\sigma_\theta) + \frac{1}{3}\Omega c_s \\ \varepsilon_\theta = \frac{1}{E}[(1 - \nu)\sigma_\theta - \nu\sigma_r] + \frac{1}{3}\Omega c_s \end{cases} \quad (8)$$

where ε_r and ε_θ are the radial and tangential strain components, σ_r and σ_θ are the radial and tangential stress components (Pa), E is the Young's modulus (Pa), ν is the Poisson's ratio, Ω is the partial molar volume of lithium ($\text{mol}\cdot\text{m}^{-3}$), and Δc_s is the change in lithium concentration in the solid phase ($\text{mol}\cdot\text{m}^{-3}$).

For an equivalent spherical particle of the active material, the strain versus displacement is given by

$$\begin{cases} \varepsilon_r = \frac{d\mu}{dr} \\ \varepsilon_\theta = \frac{\mu}{r} \end{cases} \quad (9)$$

where μ is the radial displacement (m), r is the radial coordinate (m), ε_r is the radial strain, and ε_θ is the tangential strain.

During Li insertion, the absence of external forces on the particle surface results in a radial stress of zero. Moreover, there exists a finite stress magnitude at the particle center.

Given that the diffusion rate of lithium ions within the electrode material significantly lags behind the rate of elastic deformation, the diffusion process is treated as a quasi-static equilibrium problem, formulated by Equation (10).

$$\frac{d\sigma_r}{dr} = \frac{2}{r}(\sigma_\theta - \sigma_r) \quad (10)$$

where σ_r is the radial stress (Pa), σ_θ is the tangential stress (Pa), r is the radial coordinate (m), and $d\sigma_r/dr$ is the gradient of radial stress along the particle radius.

Because the radial stress at the surface of the electrode particles is zero, and the radial and tangential stresses are approximately equal at the particle center, the boundary conditions for the static equilibrium equation:

$$\begin{cases} \sigma_r(R_p) = 0 \\ \left. \frac{d\sigma_r}{dr} \right|_{r=0} = 0 \end{cases} \quad (11)$$

where σ_r is the radial stress (Pa), R_p is the particle radius (m), and r is the radial coordinate (m). The first condition indicates that the radial stress vanishes at the particle surface, while the second condition ensures symmetry at the particle center.

Based on the aforementioned derivation, the radial and tangential stresses of the electrode particles can be determined, as depicted by Equation (12).

$$\begin{cases} \sigma_r(r) = \frac{2}{9} \frac{E\Omega[c_{av}(R_p) - c_{av}(r)]}{1 - \nu} \\ \sigma_\theta(r) = \frac{2}{9} \frac{E\Omega[2c_{av}(R_p) + c_{av}(r) - 3c(r)]}{1 - \nu} \end{cases} \quad (12)$$

where $\sigma_r(r)$ and $\sigma_\theta(r)$ are the radial and tangential stresses (Pa), E is the Young's modulus (Pa), ν is the Poisson's ratio, Ω is the partial molar volume of lithium ($\text{m}^3\cdot\text{mol}^{-1}$), $c_{av}(R_p)$ is the average lithium concentration within a particle of radius R_p ($\text{mol}\cdot\text{m}^{-3}$), $c_{av}(r)$ is the average concentration within radius r , and $c(r)$ is the local lithium concentration in the solid phase ($\text{mol}\cdot\text{m}^{-3}$).

$c_{av}(r) = \frac{3}{r^3} \int_0^r c_s(r)r^2 dr$ represents the average concentration within a spherical volume with a radius of r ($r < R_p$). Because $\lim_{r \rightarrow 0} c_{av}(r) = c_s(0)$, the expression for Equation (13) is obtained as follows:

$$\lim_{r \rightarrow 0} \sigma_r(r) = \lim_{r \rightarrow 0} \sigma_\theta(r) = \frac{2E\Omega}{9(1 - \nu)}(c_{av}(R_p) - c_s(0)) \quad (13)$$

where $c_s(0)$ is the lithium concentration at the particle center ($\text{mol}\cdot\text{m}^{-3}$). This expression represents the hydrostatic stress at the particle center.

According to (13), the stress at the center of the sphere is hydrostatic pressure.

TABLE 1 | The main equations of the P2D model.

Differential equations	Boundary conditions
<p>Solid phase diffusion</p> $\frac{\partial c_s(r, t)}{\partial t} = \frac{D_{s,y}}{r^2} \frac{\partial}{\partial r} \left(r^2 \frac{\partial c_{s,y}(r, t)}{\partial r} \right)$ <p>Electrolyte phase diffusion</p> $\varepsilon_e \frac{\partial c_e(x, t)}{\partial t} = \frac{\partial}{\partial x} \left(D_{e,y}^{\text{eff}} \frac{\partial c_e(x, t)}{\partial x} \right) + \frac{1 - L_+}{F} \frac{3\varepsilon_{s,y}}{R_{s,y}} j_{\text{tot},y}$ <p>Solid phase charge conservation</p> $-\sigma_s^{\text{eff}} \frac{\partial \phi_s}{\partial x} = i_s$ <p>Electrolyte phase conservation</p> $\frac{\partial}{\partial x} \left(\kappa_e^{\text{eff}} \frac{\partial \phi_e(x, t)}{\partial x} \right) + \frac{\partial}{\partial x} \left[\frac{2RT\kappa_e^{\text{eff}}(l_+ - l_-)}{F} \right] = -j_{\text{tot}}(t)$ <p>Kirchhoff's current law</p> $i_{\text{app}} = i_s + i_e$	<p> $c_s(r, t)$: lithium concentration in the solid phase at radial coordinate r ($\text{mol}\cdot\text{m}^{-3}$) $D_{s,y}$: solid-phase diffusion coefficient ($\text{m}^2\cdot\text{s}^{-1}$) r: radial coordinate inside the particle (m) t: time (s) </p> <p>(1)</p> <p> ε_e: electrolyte porosity (–) $c_e(x, t)$: lithium-ion concentration in electrolyte at position x ($\text{mol}\cdot\text{m}^{-3}$) D_e^{eff}: effective electrolyte diffusion coefficient ($\text{m}^2\cdot\text{s}^{-1}$) l_+: transference number of lithium-ion (–) F: Faraday constant ($\text{C}\cdot\text{mol}^{-1}$) j_{Li}: molar flux of lithium ions ($\text{A}\cdot\text{m}^{-2}$) </p> <p>(2)</p> <p> σ_s^{eff}: effective electronic conductivity in the solid phase ($\text{S}\cdot\text{m}^{-1}$) ϕ_s: solid-phase potential (V) i_s: current density in the solid phase ($\text{A}\cdot\text{m}^{-2}$) κ_e^{eff}: effective ionic conductivity of electrolyte ($\text{S}\cdot\text{m}^{-1}$) ϕ_e: solid-phase potential (V) R: universal gas constant ($\text{J}\cdot\text{mol}^{-1}\cdot\text{K}^{-1}$) T: temperature (K) </p> <p>(3)</p> <p>(4)</p> <p> i_{app}: applied current density ($\text{A}\cdot\text{m}^{-2}$) i_s: current density in the solid phase ($\text{A}\cdot\text{m}^{-2}$) i_e: current density in the electrolyte phase ($\text{A}\cdot\text{m}^{-2}$) </p> <p>(5)</p>

(Continues)

TABLE 1 | (Continued)

Differential equations	Boundary conditions
Electrochemical Kinetics	
$j_{\text{int},y} = i_{0,\text{int}} \left[\exp\left(\frac{\alpha_{a,\text{int}} F}{RT} \eta_{\text{int},y}\right) - \exp\left(-\frac{\alpha_{c,\text{int}} F}{RT} \eta_{\text{int},y}\right) \right]$ $i_{0,\text{int}} = k_{\text{int}} F \left(\frac{c_e}{c_{e,\text{ref}}} \right)^{\alpha_{a,\text{int}}} (c_{s,y,\text{max}} - c_{s,y,\text{surf}})^{\alpha_{a,\text{int}}} c_{s,y,\text{surf}}^{\alpha_{c,\text{int}}}$ $\eta_{\text{int},y} = \phi_{s,y} - \phi_e - U_{\text{int},y} - F j_{\text{int},y} R_{\text{film}}$	$j_{\text{int}}: \text{interfacial current density (A}\cdot\text{m}^{-2})$ $i_0: \text{exchange current density (A}\cdot\text{m}^{-2})$ $\alpha_a, \alpha_c: \text{anodic and cathodic charge transfer coefficients (-)}$ $F: \text{Faraday constant (C}\cdot\text{mol}^{-1})$ $R: \text{universal gas constant (J}\cdot\text{mol}^{-1}\cdot\text{K}^{-1})$ $T: \text{temperature (K)} \eta = \phi_s - \phi_e - U: \text{overpotential (V)}$ $U: \text{equilibrium potential (V)}$

(6)

When the von Mises stress of the electrode particle reaches the yield stress limit of the material, yielding occurs. In the stress tensor of a spherical particle, $\sigma_r(r) = \sigma_\phi(r)$, thus, its specific expression is:

$$\begin{aligned} \sigma_e(r) &= \sqrt{\frac{(\sigma_r(r) - \sigma_\theta(r))^2 + (\sigma_r(r) - \sigma_\phi(r))^2 + (\sigma_\theta(r) - \sigma_\phi(r))^2}{2}} \\ &= |\sigma_r(r) - \sigma_\theta(r)| \\ &= \left| \frac{E\Omega}{3(1-\nu)} (c_{\text{av}}(r) - c_s(r)) \right| \end{aligned} \quad (14)$$

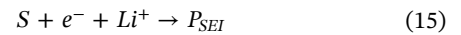
where $\sigma_e(r)$ is the von Mises equivalent stress (Pa), $\sigma_\phi(r)$ is the hoop stress (equal to σ_θ for spherical symmetry), $c_{\text{av}}(r)$ is the average concentration within radius r ($\text{mol}\cdot\text{m}^{-3}$), and $c_s(r)$ is the local lithium concentration at radius r ($\text{mol}\cdot\text{m}^{-3}$).

2.3 | SEI Growth Model

The primary degradation modes observed during battery operation are loss of active material (LAM) and loss of lithium ions (LLI) [66]. Among the various factors that contribute to battery aging, LLI, as manifested in the growth of the SEI and lithium plating, is regarded as the primary cause. Visual inspection through battery disassembly experiments reveals the absence of lithium plating on the negative electrode of the tested batteries. Moreover, under high temperature conditions, lithium plating is difficult to occur. Therefore, this study identifies SEI as the primary aging factor.

The electrolytes of LIBs typically consist of organic carbonate compounds like EC and dimethyl carbonate (DMC). During the charge-discharge cycles, electrolyte reacts with the electrode surface, resulting in the formation of solid products including polymerized organic solvents, alkaline carbonates and lithium salt precipitates. SEI forms on the negative electrode surface, with its development being most pronounced during the initial cycling. It functions to stabilize the negative electrode surface, preventing electrolyte from further decomposition, while also constraining the diffusion of lithium ions and other electrolyte components. However, the continuous growth of the SEI layer persists throughout the battery's lifespan, leading to irreversible capacity degradation.

Presently, various models have been devised for simulating SEI growth, including kMC [56, 67, 68], AIMD [69] and the kinetic limited electrochemical model [70], etc. In this study, to quantify the capacity degradation stemming from SEI growth, we assume that the formation of SEI is the reaction of the electrolyte with lithium ions and EC. This side reaction has the general form as shown in Equation (15):



where S represents the solvent, and P_{SEI} is the product formed in the reaction. The generation of SEI leads to the loss of cyclable lithium in the battery, increasing in the resistance and a decrease in the electrolyte volume fraction in the negative electrode.

Assuming that the SEI membrane growth process is irreversible, the SEI generation process is influenced by the concentration of EC on the surface of the negative electrode particles as well as the kinetics of the electrochemical reaction, following the Tafel equation as (16).

$$j_{SEI} = -\frac{i_{0,SEI}}{F} \exp\left[-\frac{\alpha_{SEI}F}{RT}\left(\phi_{s,n} - \phi_e - U_{SEI} - \frac{j_{tot}}{a}R_{SEI}\right)\right] \quad (16)$$

where j_{SEI} is the side-reaction current density for SEI formation ($A \cdot m^{-2}$), $i_{0,SEI}$ is the SEI exchange current density ($A \cdot m^{-2}$), F is the Faraday constant ($C \cdot mol^{-1}$), α_{SEI} is the charge transfer coefficient for the SEI reaction, R is the universal gas constant ($J \cdot mol^{-1}$), T is the absolute temperature (K), $\phi_{s,n}$ is the solid potential of the negative electrode (V), ϕ_e is the electrolyte potential (V), U_{SEI} is the equilibrium potential of the SEI formation reaction (V), j_{tot} is the total interfacial current density ($A \cdot m^{-2}$), a is the specific surface area of the electrode ($m^2 \cdot m^{-3}$), and R_{SEI} is the SEI film resistance ($\Omega \cdot m^2$).

1. Kinetic Limited Reaction Model

In typical electrochemical models considering battery aging, SEI growth models based on kinetic constraints are often employed [71]. However, this model fails to adequately describe the characteristic of SEI growth rate slowing down with increasing cycle numbers. Wickramanayake et al. [64] comprehensively compared a kinetic limited SEI growth model with a diffusion limited SEI growth model. The diffusion-limited model demonstrated the same linear behavior as the kinetic model. However, as the SEI layer becomes thicker, the growth rate decreases.

2. Diffusion Limited Reaction Model

The diffusion-limited SEI growth model considers the diffusion of solvents from the SEI layer/electrolyte interface to the SEI layer/anode surface [72]. Therefore, it can better model the gradual slowing down of SEI growth [73]. The model for the SEI exchange current term is as follows:

$$i_{0,SEI} = Fk_{SEI}c_{EC}(x, R_n, t)^{\alpha_{SEI}} \quad (17)$$

where $c_{EC}(x, R_n, t)$ is the EC concentration at the anode particle interface, k_{SEI} is the SEI reaction rate, and α_{SEI} is the SEI reaction transfer coefficient.

The diffusion of solvents through the SEI layer follows Fick's second law:

$$\frac{\partial c_{EC}(x, r, t)}{\partial t} = D_{sol} \frac{\partial^2 c_{EC}(x, r, t)}{\partial r^2} \quad (18)$$

where $c_{EC}(x, r, t)$ is the solvent concentration within the SEI layer ($mol \cdot m^{-3}$), D_{sol} is the solvent diffusion coefficient in the SEI ($m^2 \cdot s^{-1}$), t is time (s), and r is the radial coordinate (m).

Equation (18) holds for the following boundary conditions at the anode particle surface:

$$D_{sol} \frac{\partial c_{EC}(x, r, t)}{\partial r} \Big|_{r=R_n} = j_{SEI}(x, t) \quad (19)$$

where D_{sol} is the solvent diffusion coefficient in the SEI layer ($m^2 \cdot s^{-1}$), $c_{EC}(x, r, t)$ is the solvent concentration within the SEI ($mol \cdot m^{-3}$), r is the radial coordinate (m), R_n is the negative electrode particle radius (m), and $j_{SEI}(x, t)$ is the solvent flux consumed by SEI formation ($m^2 \cdot s^{-1}$).

Assuming that the SEI layer is a porous structure, the liquid electrolyte fills the voids within the SEI structure and reaches the electrode surface. Therefore, the effective solvent concentration at the electrolyte/SEI interface determines the boundary conditions of the equation as follows:

$$c_{EC}(x, R_n + L_{SEI}, t) = \varepsilon_{SEI} c_{0,EC} \quad (20)$$

where ε_{SEI} is the porosity of SEI layer, $c_{0,EC}$ is the bulk solution concentration.

Finally, the definitions of SEI growth and capacity decay are as follows:

$$j_{SEI}(x, t) = -\frac{n_{SEI}\rho_{SEI}}{M_{SEI}} \frac{dL_{SEI}}{dt} \quad (21)$$

$$\frac{\partial Q_{lost}(x, t)}{\partial t} = -\frac{Fa_n}{n_{SEI}} j_{SEI} \quad (22)$$

where j_{SEI} is the side-reaction current density for SEI formation ($A \cdot m^{-2}$), n_{SEI} is the number of electrons transferred in the SEI formation reaction (dimensionless), ρ_{SEI} is the density of the SEI layer ($kg \cdot m^{-3}$), M_{SEI} is the molar mass of the SEI product ($kg \cdot mol^{-1}$), and L_{SEI} is the thickness of the SEI layer (m). Q_{lost} is the capacity lost due to SEI formation ($C \cdot m^{-3}$), F is the Faraday constant ($C \cdot mol^{-3}$), and a_n is the specific surface area of the negative electrode ($m^2 \cdot m^{-3}$).

2.4 | Negative Electrode Particle Cracking

Mechanical degradation occurs in electrode particles due to stress induced by diffusion. The rate and saturation level of damage growth are contingent upon particle size and charge-discharge rates. Given the decaying trend observed in the evolution rate of microcracks, an exponential decay model is utilized in this study to estimate the density of microcracks f_{bb} [74].

$$f_{bb} = f(C_{rate}, R_s, Ahtp) = A_{max}(1 - \exp(-m_{rate} \cdot Ahtp)) \quad (23)$$

where A_{max} is the maximum potential damage in active particles, while m_{rate} is the rate of damage evolution. Both parameters are dependent on the particle radius and C-rate [74].

$$A_{\max} = -0.5902 + \frac{0.7173 + 0.0027 \cdot R_s + (-0.15/R_s)}{1 + |(0.0223 \cdot C_{\text{rate}}) - (0.2115 + (-0.002) \cdot R_s)|} \quad (24)$$

$$m_{\text{rate}} = 1.9572 + \left(1 + (-0.2058) \cdot C_{\text{rate}} + \frac{22.5694}{C_{\text{rate}}} + \frac{(-21.7787)}{(C_{\text{rate}})^2} \right) \left(1 + \frac{(-7.6826)}{R_s} + \frac{19.8345}{R_s^2} + (-0.0544) \cdot R_s \right) \quad (25)$$

where A_{\max} is the maximum potential damage in active particles (dimensionless), R_s is the particle radius (μm), and C_{rate} is the applied charge/discharge rate (h^{-1}). m_{rate} is the rate of damage evolution (dimensionless), C_{rate} is the C-rate of cycling (h^{-1}), and R_s is the particle radius (μm).

The formation of microcracks increases the tortuosity of diffusion pathways, leading to a decrease in the diffusion rate of active particles.

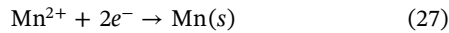
$$D_s^{\text{eff}} = D_s(1 - f_{bb})^\gamma \quad (26)$$

D_s^{eff} represents the effective solid-phase diffusion coefficient of lithium ions in the active material, while D_s denotes the intrinsic diffusion coefficient of the solid phase. The term f_{bb} refers to the microcrack density or fraction of broken bonds, and γ is the tortuosity exponent describing how microcracks increase the diffusion path length and reduce the effective diffusion rate.

2.5 | Deposition of Active Material

Although dissolution and deposition of LMO, LCO, and LNO occur at high temperature, leading to capacity degradation in batteries, evidence suggests that, due to poor cycling performance and inadequate high temperature stability of LiMnO_2 , the dissolution of Mn and electrolyte decomposition are the primary aging factors in NCM batteries under high temperature comparing with the dissolution and deposition of LiNiO_2 and LiCoO_2 . The capacity will decrease due to Mn^{2+} reduction on the anode surface. To characterize battery aging behavior under experimental conditions, this paper developed a coupled model for Mn deposition, cathode Mn dissolution, electrolyte oxidation, and salt decomposition [75].

The deposition of Mn leads to the consumption of electrons that would otherwise have been involved in the coupling with lithium ions during insertion, consequently diminishing the number of lithium ions available for recycling. The expression representing this secondary reaction is provided below:



The deposition mechanism of Mn adheres to the Butler-Volmer expression and is modulated by the thickness of the SEI. As the SEI layer thickens, the rate of Mn deposition is expected to decline. Hence, by defining an exponential decay

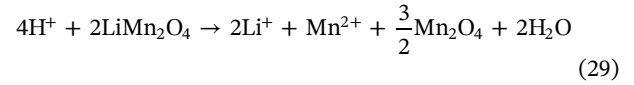
function $R(\delta)$, the current associated with manganese deposition can be described as:

$$i_{\text{Mn-dep}} = R(\delta) \cdot i_{\text{Mn-dep}}^* = -e^{-\lambda_{\text{Mn-dep}} \delta} F k_{\text{Mn-dep}} c_{\text{Mn}^{2+}} \exp \left[-\frac{\alpha_c^{\text{Mn-dep}} 2F}{RT} (\phi_{s,n} - \phi_e) \right] \quad (28)$$

where $i_{\text{Mn-dep}}$ denotes the current density associated with manganese deposition, while $R(\delta)$ is an exponential decay function that accounts for the influence of SEI thickness on the deposition process. The term $i_{\text{Mn-dep}}^*$ represents the intrinsic exchange current density for manganese deposition, $k_{\text{Mn-dep}}$ is the reaction rate constant, and $c_{\text{Mn}^{2+}}$ is the concentration of manganese ions near the anode surface. Here, $\alpha_c^{\text{Mn-dep}}$ is the charge transfer coefficient, F is the Faraday constant, R is the universal gas constant, and T is the absolute temperature. The potentials $\phi_{s,n}$ and ϕ_e correspond to the solid-phase potential of the negative electrode and the electrolyte potential, respectively.

2.6 | Dissolution of Active Material & Electrolyte Oxidation

Protons generated as a result of solvent oxidation and salt decomposition play a pivotal role in the dissolution of manganese. Under the influence of protons, lithium manganese compounds undergo oxidation, releasing Mn^{2+} ions. This reaction is depicted by Equation (29).



H^+ represents protons generated from electrolyte decomposition or solvent oxidation, and LiMn_2O_4 denotes the manganese-containing cathode material. The reaction produces Li^+ ions that participate in the normal intercalation process, while Mn^{2+} ions are released into the electrolyte due to the structural degradation of the cathode. The solid product Mn_2O_4 and water (H_2O) are also formed as secondary products of this dissolution reaction.

According to (29), because the proton has a lower concentration, the reaction rate is controlled by the proton concentration within the cathode. Therefore, the dissolution current of manganese is given by equation:

$$i_{\text{Mn-dis}} = f_{\text{Mn-dis}} i_{\text{Mn-react}} = f_{\text{Mn-dis}} F k_{\text{dis}} c_{\text{H}^+} \quad (30)$$

where $i_{\text{Mn-dis}}$ is the Mn dissolution rate, $f_{\text{Mn-dis}}$ is the fraction coefficient, $i_{\text{Mn-react}}$ is the reaction rate, k_{dis} is the reaction rate.

The H^+ originates from solvent oxidation and salt decomposition. The solvent oxidation equation is given below:



Assuming that the solvent oxidation is irreversible, the exchange flux of solvent oxidation follows the Tafel equation:

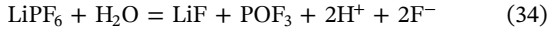
$$j_{\text{oxid}} = a_c i_0^{\text{sol}} \exp \left[\frac{\alpha_a^{\text{sol}} F}{RT} (\phi_{s,n} - \phi_e - U_{\text{oxid}}^{\text{eq}}) \right] \quad (32)$$

where j_{oxid} denotes the current density of solvent oxidation, and a_c is the specific surface area of the electrode. The term i_0^{sol} represents the exchange current density for solvent oxidation, while α_a^{sol} is the anodic charge transfer coefficient. Here, F is the Faraday constant, R is the universal gas constant, and T is the absolute temperature. The potentials $\phi_{s,n}$ and ϕ_e correspond to the solid-phase potential of the negative electrode and the electrolyte potential, respectively, and $U_{\text{oxid}}^{\text{eq}}$ is the equilibrium potential of the solvent oxidation reaction.

Assuming that the current for proton production from solvent oxidation is a small fraction of the oxidation current, therefore:

$$j_{\text{H}^+}^{\text{oxid}} = f_{\text{H}^+} \cdot j_{\text{oxid}} \quad (33)$$

Another source of protons is the reaction between the electrolyte salt lithium hexafluorophosphate (LiPF_6) and H_2O , which generates H^+ , as expressed in Equation (27). This process does not consume Mn from the positive electrode or recyclable Li^+ ions in the electrolyte; it simply involves the generation of H^+ .



Due to the decomposition of LiPF_6 , the H^+ production is controlled by:

$$j_{\text{H}^+}^{\text{salt}} = F k_{\text{decom}} (c_{\text{H}_2\text{O}})^2 c_{\text{LiPF}_6} \quad (35)$$

where $j_{\text{H}^+}^{\text{eff}}$ is the current density of proton production from LiPF_6 decomposition ($\text{A}\cdot\text{m}^{-2}$), F is the Faraday constant ($\text{C}\cdot\text{mol}^{-1}$), k_{decom} is the reaction rate constant for LiPF_6 decomposition ($\text{m}^6\cdot\text{mol}^{-2}\cdot\text{s}^{-1}$), $c_{\text{H}_2\text{O}}$ is the water concentration in the electrolyte ($\text{mol}\cdot\text{m}^{-3}$), and c_{LiPF_6} is the concentration of LiPF_6 salt in the electrolyte ($\text{mol}\cdot\text{m}^{-3}$).

Since the concentrations of Mn^{2+} and H^+ are relatively low, the effect of potential on the migration is neglected and only diffusion is present. In summary, the concentration changes of H^+ and Mn^{2+} are modeled as follows (36) with the following boundary conditions (37)

$$\begin{cases} \varepsilon_2^{\text{pos}} \frac{\partial c_{\text{H}^+}}{\partial t} = \nabla \cdot (D_{\text{H}^+}^{\text{eff}} \nabla c_{\text{H}^+}) + \frac{1}{F} (j_{\text{H}^+}^{\text{salt}} - 4a_s^{\text{pos}} i_{\text{Mn react}}) \\ \varepsilon_2^{\text{sep}} \frac{\partial c_{\text{H}^+}}{\partial t} = \nabla \cdot (D_{\text{H}^+}^{\text{eff}} \nabla c_{\text{H}^+}) + \frac{j_{\text{H}^+}^{\text{salt}}}{F} \\ \varepsilon_2^{\text{neg}} \frac{\partial c_{\text{H}^+}}{\partial t} = \nabla \cdot (D_{\text{H}^+}^{\text{eff}} \nabla c_{\text{H}^+}) + \frac{1}{F} (j_{\text{H}^+}^{\text{salt}} + a_s^{\text{neg}} i_{\text{H}_2}) \\ \varepsilon_2^{\text{pos}} \frac{\partial c_{\text{Mn}^{2+}}}{\partial t} = \nabla \cdot (D_{\text{Mn}^{2+}}^{\text{eff}} \nabla c_{\text{Mn}^{2+}}) + \frac{1}{F} a_s^{\text{pos}} i_{\text{Mn dis}} \\ \varepsilon_2^{\text{sep}} \frac{\partial c_{\text{Mn}^{2+}}}{\partial t} = \nabla \cdot (D_{\text{Mn}^{2+}}^{\text{eff}} \nabla c_{\text{Mn}^{2+}}) \\ \varepsilon_2^{\text{neg}} \frac{\partial c_{\text{Mn}^{2+}}}{\partial t} = \nabla \cdot (D_{\text{Mn}^{2+}}^{\text{eff}} \nabla c_{\text{Mn}^{2+}}) + \frac{1}{F} a_s^{\text{neg}} i_{\text{Mn dep}} \end{cases} \quad (36)$$

$$\begin{cases} \left. \frac{\partial c_{\text{Mn}^{2+}}}{\partial x} \right|_{x=0} = \left. \frac{\partial c_{\text{Mn}^{2+}}}{\partial x} \right|_{x=L} = 0 \\ \left. \frac{\partial c_{\text{H}^+}}{\partial x} \right|_{x=0} = \left. \frac{\partial c_{\text{H}^+}}{\partial x} \right|_{x=L} = 0 \end{cases} \quad (37)$$

where $\varepsilon_2^{\text{pos}}$, $\varepsilon_2^{\text{sep}}$, and $\varepsilon_2^{\text{neg}}$ are the volume fractions of electrolyte in the positive electrode, separator, and negative electrode (dimensionless), c_{H^+} is the concentration of protons ($\text{mol}\cdot\text{m}^{-3}$), $j_{\text{H}^+}^{\text{eff}}$ is the effective diffusion coefficient of protons ($\text{m}^2\cdot\text{s}^{-1}$), $j_{\text{H}^+}^{\text{salt}}$ is the current density of proton generation from LiPF_6 decomposition ($\text{A}\cdot\text{m}^{-2}$), $j_{\text{H}^+}^{\text{oxid}}$ is the current density of proton generation from solvent oxidation ($\text{A}\cdot\text{m}^{-2}$), $i_{\text{Mn react}}$ is the current density of Mn-related reactions ($\text{A}\cdot\text{m}^{-2}$), i_{H_2} is the current density of hydrogen evolution ($\text{A}\cdot\text{m}^{-2}$), F is the Faraday constant ($\text{C}\cdot\text{mol}^{-1}$), and a_s^{pos} are the specific surface areas of the positive and negative electrodes ($\text{m}^2\cdot\text{m}^{-3}$). $c_{\text{Mn}^{2+}}$ is the concentration of dissolved manganese ions ($\text{mol}\cdot\text{m}^{-3}$), $D_{\text{Mn}^{2+}}^{\text{eff}}$ is the effective diffusion coefficient of Mn^{2+} ($\text{m}^2\cdot\text{s}^{-1}$), $i_{\text{Mn dis}}$ is the current density of Mn dissolution ($\text{A}\cdot\text{m}^{-2}$), and $i_{\text{Mn dep}}$ is the current density of Mn deposition ($\text{A}\cdot\text{m}^{-2}$).

According to the hypothesis, Mn dissolution is the primary aging factor under high temperature conditions. However, the LAM caused solely by Mn dissolution cannot fully explain the overall capacity degradation. Therefore, considering the use of solid phase volume fraction and defining effective volume fraction, is proposed to describe the attenuation caused by Mn dissolution and deposition.

$$\begin{cases} \frac{\partial \varepsilon_{s,p}}{\partial t} = -\frac{a_{s,p} i_{\text{Mn react}} \bar{V}}{F} \\ \frac{d \varepsilon_{s,p}^{\text{eff}}}{dt} = k_{\text{iso}} \frac{d \varepsilon_{s,p}}{dt} \end{cases} \quad (38)$$

where $\varepsilon_{s,p}$ is the solid phase volume fraction of active material in the positive electrode (dimensionless), $a_{s,p}$ is the specific surface area of the positive electrode ($\text{m}^2\cdot\text{m}^{-3}$), and $i_{\text{Mn react}}$ is the current density of Mn-related reaction ($\text{A}\cdot\text{m}^{-2}$). \bar{V} is the molar volume of the electrode material ($\text{m}^3\cdot\text{mol}^{-1}$), F is the Faraday constant ($\text{C}\cdot\text{mol}^{-1}$), and $\varepsilon_{s,p}^{\text{eff}}$ is the effective solid volume fraction after reaction (dimensionless). k_{iso} is the isotropic correction coefficient (dimensionless), and t is the time (s).

Assuming that the LAM is primarily driven by Mn and occurs throughout the electrode, \bar{V} represents the molar volume of the positive electrode material.

After the LAM occurs, both the maximum lithium capacity and effective lithium capacity per unit electrode volume decrease. In the absence of specific reaction equations for these two aging modes, it is sufficient to adjust the model parameters to achieve an adequate simulation to the effects of Co, Ni and Mn dissolution and deposition on battery life in the same time.

$$\begin{cases} c_{\text{Li},p,\text{max}} = \varepsilon_{s,p}^{\text{eff}} c_{\text{Li},p,\text{max}} \\ c_{\text{Li},p,\text{eff}} = \varepsilon_{s,p} c_{\text{Li},p,0} \end{cases} \quad (39)$$

$$\begin{cases} j_{\text{tot},n} = j_{n,\text{int}}(t) + j_{\text{SEI}}(t) + a_a i_{\text{Mn dep}} \\ j_{\text{tot},p} = j_{p,\text{int}}(t) - j_{\text{oxid}}(t) + 2a_a i_{\text{Mn react}} \end{cases} \quad (40)$$

where $c_{Li,p,max}$ is the maximum lithium concentration in the positive electrode ($\text{mol}\cdot\text{m}^{-3}$), $\varepsilon_{s,p}^{\text{eff}}$ is the effective solid-phase volume fraction of the positive electrode (dimensionless), and $c_{Li,p,0}$ is the initial lithium concentration in the positive electrode ($\text{mol}\cdot\text{m}^{-3}$). $j_{\text{tot},n}$ is the total interfacial current density in the negative electrode ($\text{A}\cdot\text{m}^{-2}$), $j_{n,\text{int}}(t)$ is the intercalation current density of the negative electrode ($\text{A}\cdot\text{m}^{-2}$), and j_{SEI} is the side-reaction current density for SEI formation ($\text{A}\cdot\text{m}^{-2}$). a_d is the specific surface area of the electrode ($\text{m}^2\cdot\text{m}^{-3}$), and i_{Mn_dep} is the current density of manganese deposition ($\text{A}\cdot\text{m}^{-2}$). $j_{\text{tot},p}(t)$ is the total interfacial current density in the positive electrode ($\text{A}\cdot\text{m}^{-2}$), $j_{p,\text{int}}(t)$ is the intercalation current density of the positive electrode ($\text{A}\cdot\text{m}^{-2}$), $j_{\text{oxid}}(t)$ is the current density of solvent oxidation ($\text{A}\cdot\text{m}^{-2}$), and $i_{\text{Mn}_\text{react}}$ is the current density of manganese-related reactions ($\text{A}\cdot\text{m}^{-2}$).

The above aging mechanisms are coupled directly to the electrochemical model via current relationships, as (40).

The parameters used in the model are consistent with commonly reported values in the literature and were chosen to remain physically meaningful and within reasonable ranges. Their suitability for the present system was evaluated by comparing model predictions with experimental cycling data at 60°C , ensuring that the framework reflects realistic degradation behavior without requiring extensive parameter re-identification.

3 | Experimental Section

3.1 | High Temperature Battery Aging Experiment

The 18650-battery used in this study features an NCM523-based positive electrode, with a rated capacity of 2.9 Ah and a nominal voltage of 4.2 V. All charging/discharging procedures were performed at a controlled temperature of 60°C . The experimental protocol began with an initial constant current-constant voltage (CC-CV) charge to 100% SOC, followed by a 10-min rest period. The battery was then discharged at 1 C to 50% SOC to establish a baseline condition. The subsequent cycling tests consisted of repeated 0.5 C charging to 85% SOC, a 10-min rest, 1 C discharging to 50% SOC, and another 10-min rest interval. The current and voltage profiles for the initial cycles are presented in Figure 2, demonstrating the characteristic behavior during these operational phases. This cycling regimen was maintained for 1250 full cycles to evaluate long-term performance under the specified conditions.

3.2 | Battery Disassembly Experiment

To understand the aging-related reactions inside the cell, it is necessary to conduct battery disassembly experiments. The experiments are conducted inside a glovebox, and the states of battery electrodes at different aging levels are shown in Figure 3.

The batteries at different aging stages, as shown in Figure 3, demonstrate progressively severe degradation from left to right. The white region corresponds to the separator, while the deep

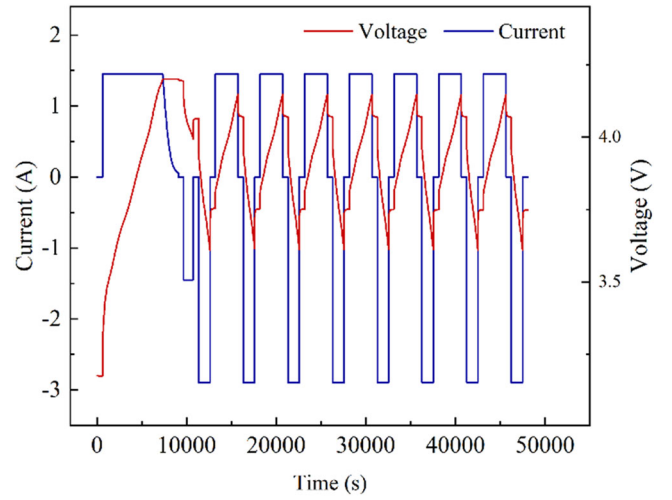


FIGURE 2 | The current and voltage curves for the first nine cycles.

black areas represent active materials (NCM523 cathode and graphite anode). The silver-white and purple-red zones denote aluminum and copper current collectors respectively, with light black deposits indicating other material accumulated on current collectors. Figure 3 reveals significant detachment of active materials from both electrodes, attributable to three synergistic degradation mechanisms under high-temperature conditions: (1) excessive drying of the electrodes, (2) binder failure, and (3) active material loss. Notably, Batteries numbered 12, 14, and 32 exhibited incomplete discharge, evidenced by lithium metal plating (metallic luster) on the anode. Post-mortem analysis confirmed that elevated temperatures accelerated electrolyte oxidation, generating gaseous byproducts that compromised tab-cap weld integrity due to volume expansion. Therefore, cells 12, 14, and 32 were tested with zero voltage, indicating cell failure. Concurrent solvent evaporation further exacerbated electrode drying, creating localized arid zones that promoted material delamination. Additionally, high temperatures caused binder softening and viscosity reduction, making electrode materials more prone to drying, detachment, and pulverization. These disassembly experiments indicate that the primary aging mechanisms during high-temperature, low-rate cycling are SEI layer growth, LAM, and electrolyte oxidation.

3.3 | Multiscale Characterization Experiments

Battery aging mechanisms under high-temperature conditions exhibit greater complexity compared to normal or low-temperature operation. Two primary degradation pathways are identified: (1) accelerated SEI growth at elevated temperatures, and (2) active material detachment caused by electrode drying, as visually confirmed in Figure 3. Through systematic disassembly of batteries aged at 60°C under controlled experimental conditions, we performed multi-scale characterization to isolate thermal degradation effects. The use of a relatively low rate during cycling eliminates lithium plating and overcharge/discharge as potential aging factors.

Figure 4 presents comparative SEM analysis of NCM523 cathode materials pre- and post-aging, revealing a positive correlation between aging severity (quantified up to 17.96% capacity loss) and

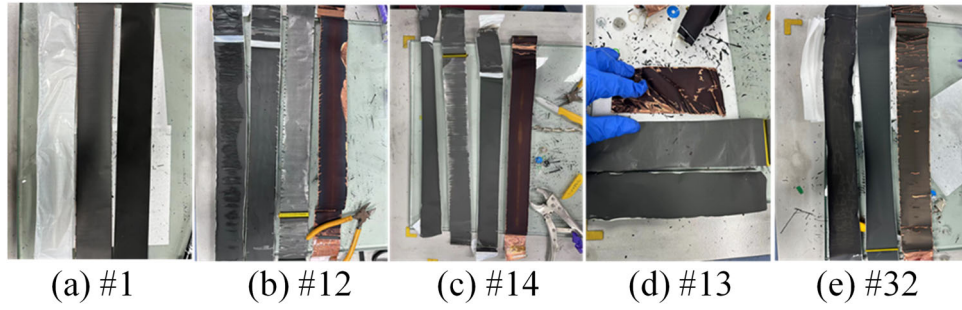


FIGURE 3 | Macroscopic morphology of batteries at each aging stage; (a) fresh battery, #1; (b) #12, SOH 86.86%; (c) #14, SOH 85.86%; (d) #13, SOH 82.56%; (e) #32, SOH 82.04%.

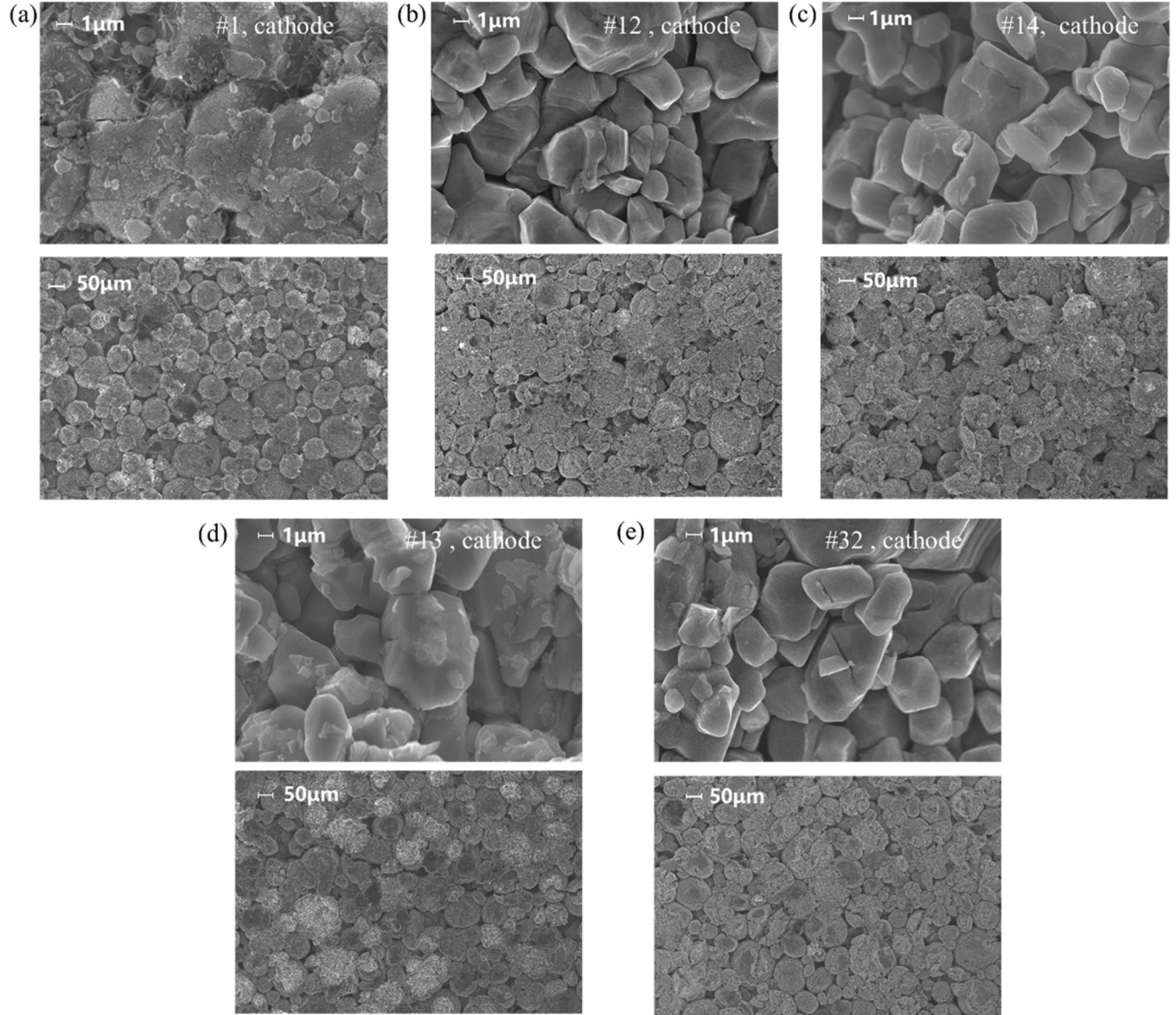


FIGURE 4 | The SEM images of NCM523 cathode material from (a) battery #1, (b) battery #12, (c) battery #14, (d) battery #13 and (e) battery #32.

the progression of surface crack formation. Pristine cathodes display binder-encapsulated primary/secondary particles with minor processing-induced cracks from electrode calendaring and winding. As aging severity increases to 17.96%, there is

noticeable growth in cracks on the electrode particle surfaces, attributed to three synergistic mechanisms: (i) PVDF binder degradation, (ii) electrode surface drying, and (iii) accumulated mechanical stress during cycling.

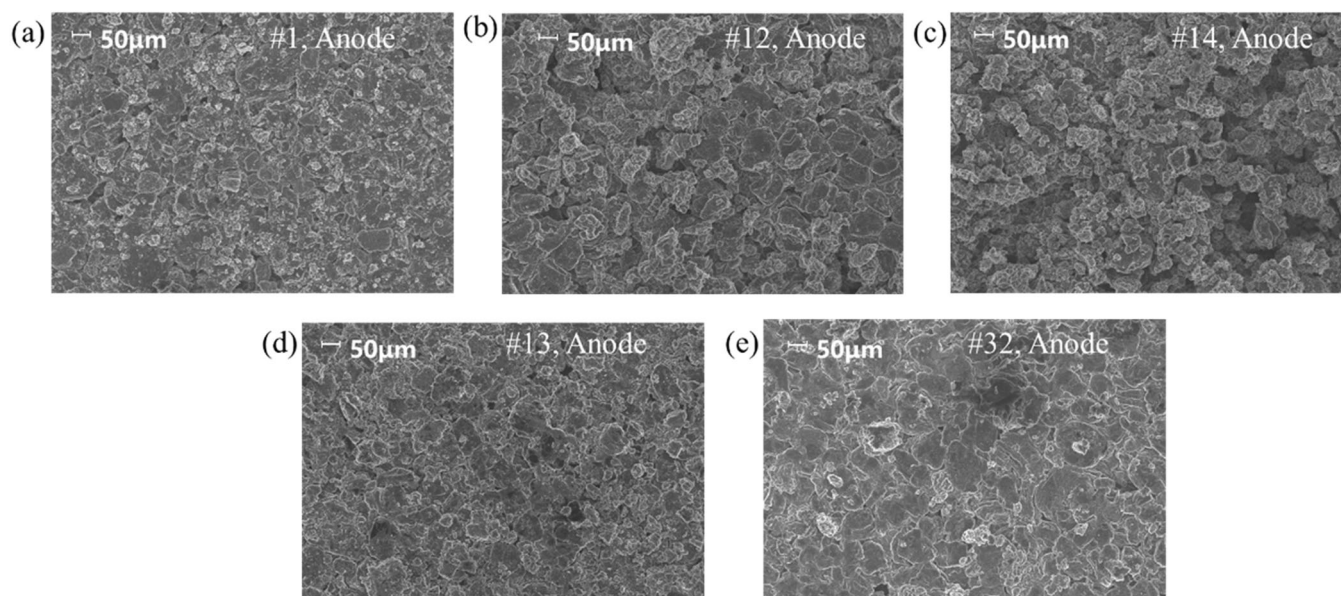


FIGURE 5 | The SEM images of anode material from (a) battery #1, (b) battery #12, (c) battery #14, (d) battery #13 and (e) battery #32.

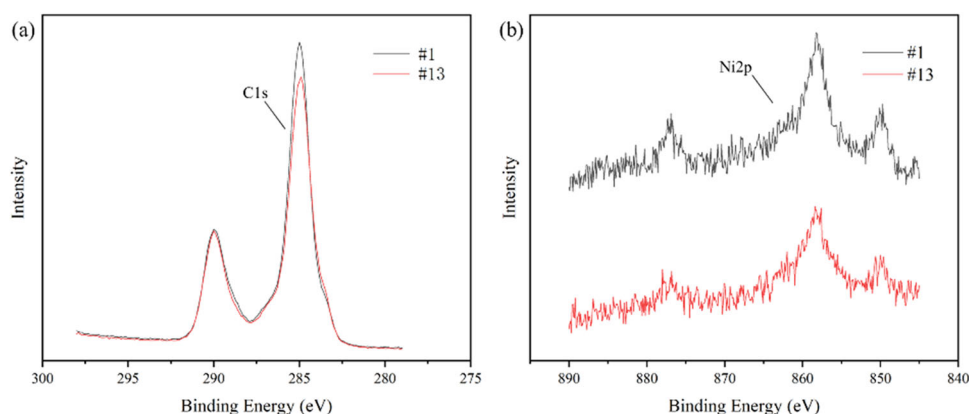


FIGURE 6 | The (a) C1s and (b) Ni2p spectra of anode material.

Complementary analysis of anode materials in Figure 5 demonstrates stress-induced irregular detachment of graphite particles, exacerbated by interfacial drying. These microstructural evolutions collectively validate the predominance of thermally-driven material degradation in the observed capacity fade.

Figure 6 illustrates the XPS spectra of the anode electrode before and after aging. The C1s pattern reveals a notable increase in the intensity of the C-Li peak following cycling. This suggests that the relative content of the C-Li compound is gradually increasing, indicating a gradual incorporation of Li into the electrode. The surface of the graphite exhibits an increase in the loss of active lithium ions, while the change in the other peak is not significant. The Ni2p pattern displays a rise in the content of Ni, indicating the presence of a transition metal at the positive electrode and its dissolution and deposition at the negative electrode.

Figure 7 depicts the XPS spectra of the cathode material before and after aging. It can be observed that the cathode is more affected by the shedding of the active material. Additionally, the Ni elemental pattern indicates that Ni^{2+} is dissolved

from the main structure. Upon entry of the cathode into the electrolyte, NiF_2 is formed on the cathode surface. The results of the spectral analysis of C1s, O1s, and F1s indicate the emergence of a CEI film on the cathode surface. The peak at 529 eV on the O1s spectrum is attributed to the appearance of lattice oxygen peaks (O-M) in the cathode material, and the peak at 532 eV is attributed to the C=O, both of which exhibit significant growth. Furthermore, the generated NiF_2 and CEI impeded further characterization of the transition metals.

As illustrated in Figure 8a,b, the XRD spectra of the electrode material at varying aging stages exhibited minimal spectral differences without emergence of new crystalline phases. The electrodes were subjected to high cycling temperatures, resulting in over-drying and the dislodgment of the material during disassembly. Therefore, the test samples of the aged battery were scraped from the electrodes. Notably, peaks related to copper (111), (200), and (220) can be only observed in the XRD spectra for cell #1, as its sample was prepared by cutting the intact negative electrode sheet. The prominent (002) peak characteristic of graphite reflects the primary crystallographic orientation of the graphite planes. As the degree of battery aging

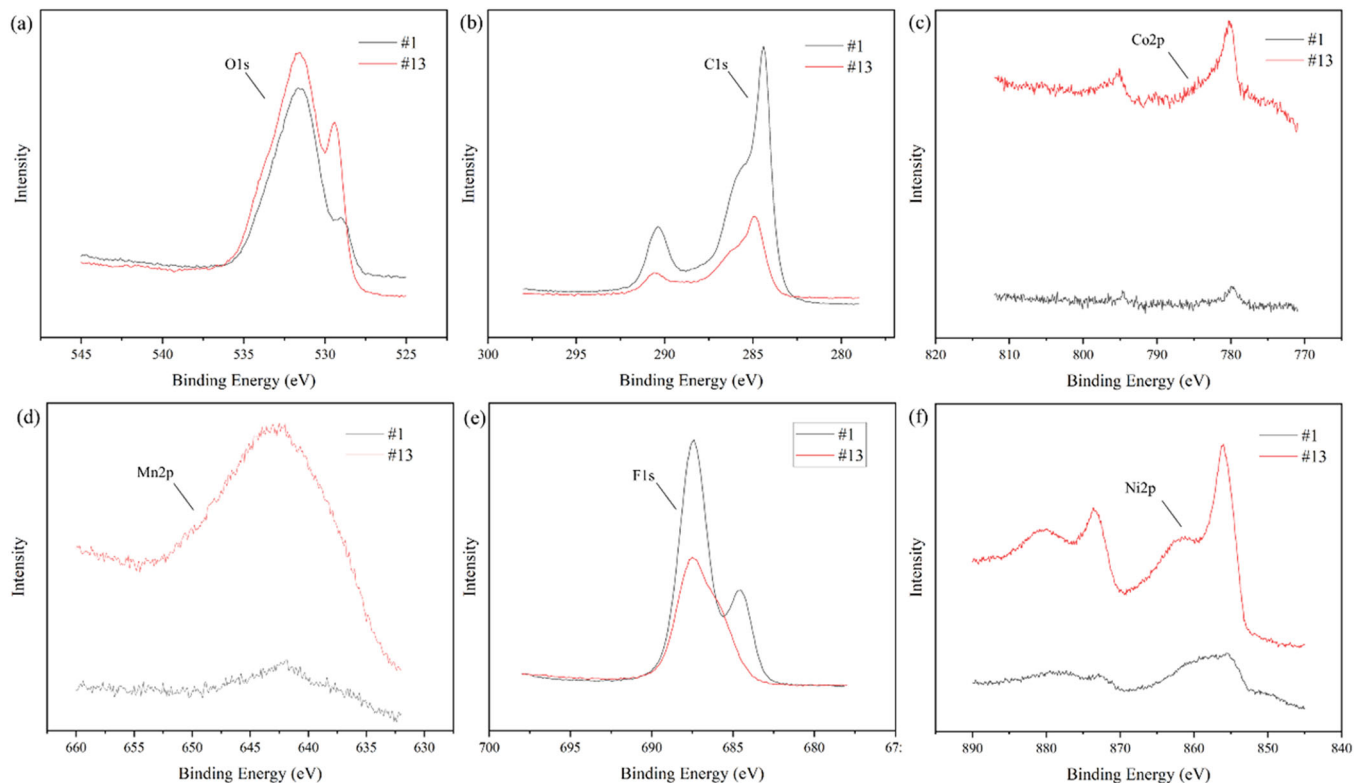


FIGURE 7 | The (a) O1s, (b) C1s, (c) Co2p, (d) Mn2p, (e) F1s and (f) Ni2p spectra of cathode material.

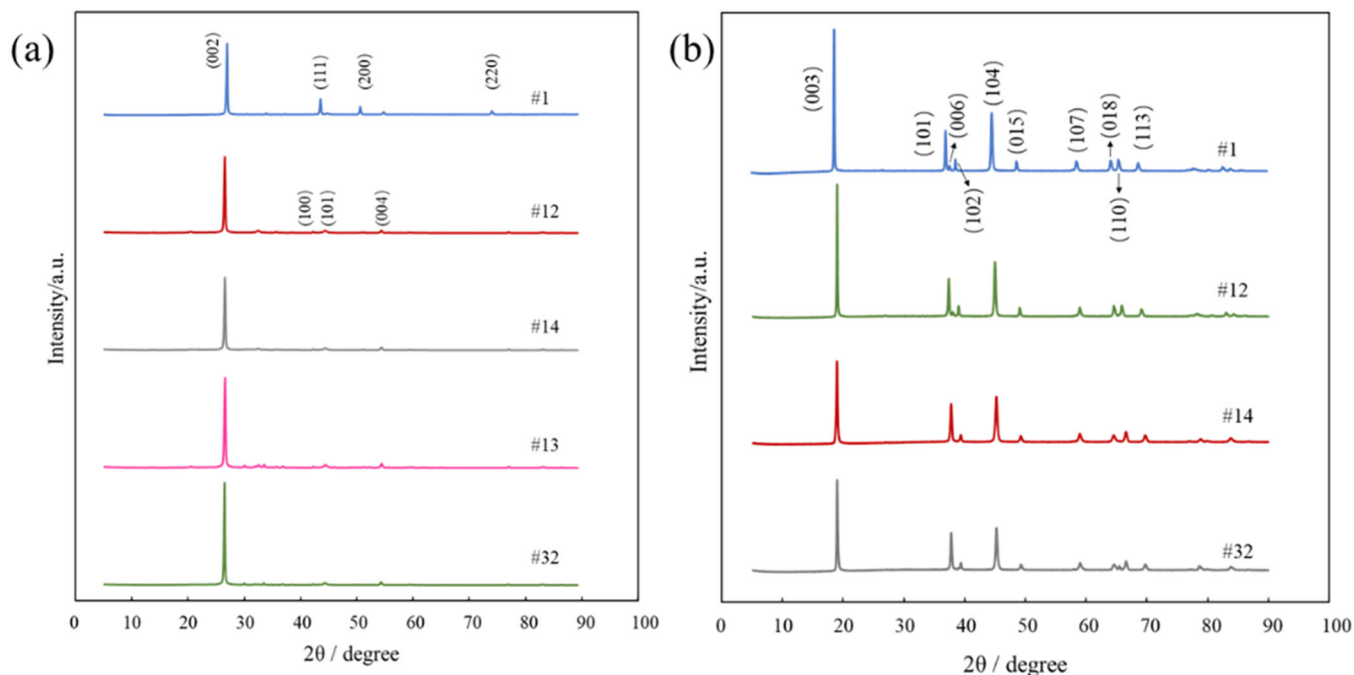


FIGURE 8 | The XRD spectra of (a) anode and (b) cathode materials.

increases, the diffraction angle 2θ gradually decreases with the (002) peak of the graphite material shifting significantly towards lower angles. According to Bragg's equation, this indicates a gradual increase in the interlayer spacing of the graphite. The Scherrer equation demonstrates that the grain size of the graphite material tends to decrease as the half-height width of the diffraction peak (002) increases. The decrease in

the particle size also indicates that the graphite material is peeling off after aging at high temperature, which is consistent with the morphology analysis of the graphite anode. These phenomena indicate a certain degree of damage to the graphite material structure. Due to the expansion of the battery caused by gas generated, the battery was not fully discharged, and the negative electrode Li existed embedded, so the (002) peak peaks

of cells 14, 13 and 32 were intensified. Figure 9 shows the XRD spectra of the new battery, battery 12, battery 14 and battery 32. Due to the severe shedding of the anode material of battery 13 and the aging degree is consistent with that of battery 32, the experiments of battery 13 are not considered for the time being. The degree of splitting of the two pairs of diffraction peaks (006) and (102) facets, and (108) and (110) facets is used to characterize the layered structure of the NCM material. According to the experimental results, there is no significant change in I003/I104, which proves that the high temperature and low multiplicity working conditions have little effect on the crystal structure of the material.

Figure 9 illustrates the Raman spectroscopy test results for anode materials at different aging stages.

The spectral comparison reveals substantial intensification of both D and D' bands with progressive aging, indicative of increased structural disorder in graphite crystallites. This disorder manifests through the emergence of sp³-hybridized carbon defects and mixed crystallographic orientations.

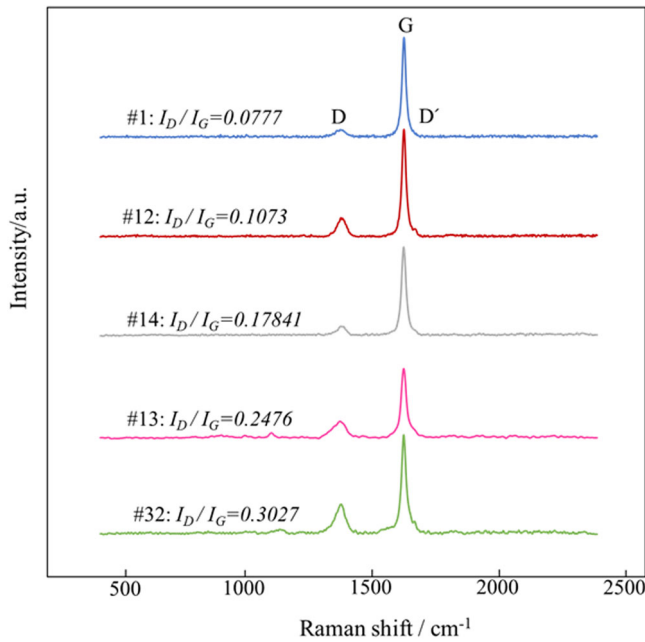


FIGURE 9 | The Raman spectra of the anode material.

Furthermore, the increasing I_D/I_G ratio (D-band to G-band intensity) quantitatively confirms the accumulation of lattice imperfections. These spectroscopic signatures collectively demonstrate the temperature-accelerated structural degradation of graphite anodes during electrochemical cycling, characterized by progressive graphitic lattice distortion and edge defect formation.

4 | Results and Discussion

The simulation results in Figure 10a demonstrate the capacity degradation trend over 2200 cycles, predicting a state-of-health (SOH) of 73.2% upon cycle completion. The simulation outcomes exhibit a maximum error of 2.5% and a root mean square error of 1.6%. Under continuous 60°C cycling conditions, the battery's end-of-life is projected at approximately 1180 cycles when reaching 80% remaining capacity, showing excellent agreement with experimental observations (1196 cycles). In terms of lifespan estimation, considering the ongoing charge-discharge conditions at 60°C, the battery is projected to retire approximately 1180 cycles, with the remaining usable capacity nearing 80%. Additionally, the simulation parameters were adjusted to obtain the capacity fade curves at different charging/discharging rates. As illustrated in Figure 10, nonlinear aging behavior and capacity knee-point persist even without lithium plating considerations. This phenomenon originates from the progressively dominant role of LAM in capacity deterioration under elevated temperatures, as confirmed by both simulation and experimental validation.

Crack propagation represents a significant mechanical degradation mechanism in battery electrodes. Under the present experimental conditions, however, crack propagation is minimal, yielding a computed value of 0 within the model. This is directly correlated with the lower charge/discharge rates and limited depth of cycling employed. To investigate rate-dependent mechanical degradation, we systematically modified the simulation parameters to evaluate crack evolution under accelerated cycling conditions (1.5 C, 2 C, 3 C, and 4 C). The simulation model was calibrated using the capacity degradation data obtained from high-temperature cycling experiments at 60°C. The predicted SOH curve and voltage response show good agreement with the experimental measurements, indicating the

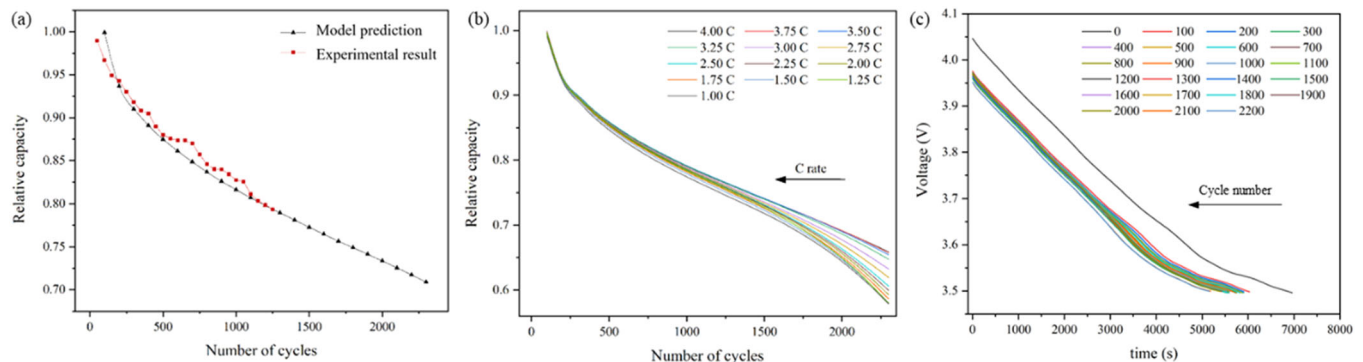


FIGURE 10 | Life prediction results. (a) Comparison of simulation results and experimental data of capacity degradation under experiment conditions; (b) Model predictions at different rates; (c) Discharge curve prediction.

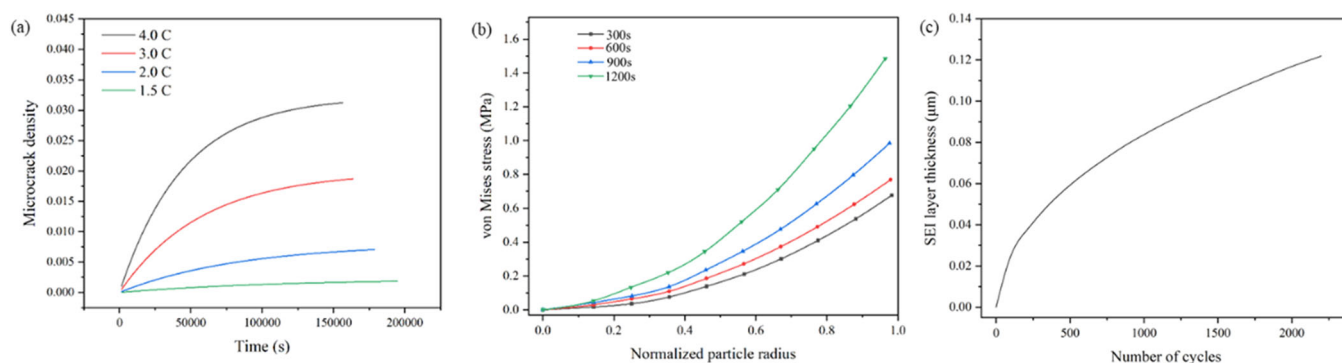


FIGURE 11 | (a) Fraction of broken bonds at different charging/discharging rates. (b) The distribution of von Mises stress within negative electrode particles during the discharge process under experimental conditions. (c) Growth of SEI layer thickness as a function of cycle number.

validity of the model under thermal aging conditions. In addition, post-mortem analyses (e.g., SEM, XPS, XRD, Raman) provide supporting evidence for the main degradation mechanisms captured in the simulation, including SEI layer growth, active material loss, and Mn dissolution/deposition. These comparisons qualitatively reinforce the reliability of the model assumptions and outputs. As shown in Figure 10a, the simulated capacity fade exhibits close agreement with the experimental data at 60°C. The predicted end-of-life cycle number closely matches the measurements, and the discharge profiles in Figure 10c further confirm the consistency between simulation and experiment. These results indicate that the adopted parameter set is appropriate for describing the behavior of the present system.

The simulation results are illustrated in Figure 11. The von Mises stress encompasses contributions from both radial and tangential components induced by diffusion. At the center of the sphere, the von Mises stress is 0, and it increases towards the surface. The equivalent stress at any position increases over time, reaching its maximum at the particle surface during the final stages of discharge. Therefore, the particle surface is most susceptible to fracture. The surface von Mises stress essentially simulates the characteristics of tangential components of diffusion-induced surface stress. As shown in Figure 11, the von Mises stress initially increases at the separator and subsequently at the current collector end. Due to concentration gradients within the porous electrode, the stress induced in electrode particles varies at different locations along with the negative electrode. Similarly, it can be envisioned that the total elastic strain density driving fracture also varies at different locations along with the negative electrode.

Assumptions made in the current modeling framework include simplified reaction kinetics, idealized coupling relationships, and the absence of explicit spatial heterogeneity. While these assumptions enable computational tractability, they also limit the model's ability to fully resolve the complex interplay between degradation pathways. Due to the lack of decoupled experimental data, the individual contribution of each side reaction cannot be directly validated. Nevertheless, the model captures the general transition in dominant aging mechanisms over time, which qualitatively agrees with widely reported high-temperature degradation behaviors. Future improvements will focus on integrating advanced in situ characterization techniques to enhance parameter calibration and isolate the effects of specific side reactions.

Overall, the consistency between model predictions and the 60°C cycling experiments demonstrates the reliability of the framework. The dominant degradation pathways represented in the model are in line with the degradation features observed in post-mortem analyses, confirming that the framework provides a realistic description of high-temperature aging mechanisms.

5 | Conclusion

This study applies a simplified electrochemical-mechanical coupling framework that incorporates five key degradation mechanisms, SEI growth, particle fracture in the negative electrode, electrolyte oxidation, dissolution of active materials, and subsequent deposition, to interpret the degradation behavior of LIBs under 60°C cycling conditions. The model accounts for temperature-dependent reaction kinetics and interactions among different degradation pathways, allowing accurate prediction of capacity fade during long-term operation under high-temperature conditions. Simulation results show strong agreement with experimental data obtained from cycling tests at 60°C, with a root mean square error of 1.6 percent. The results indicate that degradation processes evolve throughout the aging cycle. SEI growth is dominant in the early stage, while electrolyte oxidation and active material loss become the main contributors during the later stages. Post-mortem analysis confirms the presence of severe electrolyte decomposition, electrode drying, and gas evolution, providing experimental support for the model's predictions and offering insights into failure modes under thermal stress. While the current model captures the essential trends in high-temperature degradation, further development is required to improve its accuracy and adaptability. Future work will focus on establishing species-specific dissolution models for transition metals such as nickel, cobalt, and manganese, integrating stress-dependent descriptions of particle cracking, and implementing refined parameter identification methods for aging reactions. These efforts are expected to enhance the reliability and generalization of lifespan prediction tools for LIBs operating under demanding thermal environments.

Acknowledgments

This work was financially supported by the National Natural Science Foundation of China (No. 52102470), the National Natural Science

Foundation of China (No. 52302486) and National Key R&D Program of China under Grant (No. 2021YFB2501300). We also would like to thank the support from the Science and Technology Commission Foundation Strengthening Plan Fund of China.

Conflicts of Interest

The authors declare no conflicts of interest.

Data Availability Statement

The data that support the findings of this study are available from the corresponding author upon reasonable request.

References

1. D. Li, J. Liu, X. Chen, et al., "Regulation of Coordinated Nitrogen Species for Atomically Dispersed Fe-N5 Catalyst to Boost Electrocatalytic CO₂-to-Co Conversion," *Applied Catalysis B: Environment and Energy* 365 (2025): 124824.
2. F. Sher, S. Hameed, N. Smječanin Omerbegović, et al., "Cutting-Edge Biomass Gasification Technologies for Renewable Energy Generation and Achieving Net Zero Emissions," *Energy Conversion and Management* 323 (2025): 119213.
3. X. Liu, X. Tian, H. Zhang, et al., "Shifting From MOF Powder: Monoliths for Efficient Removal of Hazardous Substances," *Rare Metals* (2025), <https://doi.org/10.1007/s12598-025-03519-0>.
4. S. Li, Z. Xin, Y. Luo, et al., "Recent Advances In the Development of Single Atom Catalysts for Oxygen Evolution Reaction," *International Journal of Hydrogen Energy* 82 (2024): 1081–1100.
5. S. Zheng, Z. Feng, Y. Lu, Y. Hua, and Z. Gao, "Impact of Crosslinking in Poly(Naphthalene-Co-Terphenyl Piperidinium) Copolymer for Anion Exchange Membrane Fuel Cells," *Materials Today Communications* 45 (2025): 112242.
6. S. Li, Z. Xin, J. Han, et al., "Pt@Co-B Catalyzed Direct Borohydride Fuel Cell Anode: Rational Design and Performance Evaluation," *Ionics* 30 (2024): 7213–7222.
7. M. Khan, Z. Akmal, M. Tayyab, et al., "MOFs Materials as Photocatalysts for CO₂ Reduction: Progress, Challenges and Perspectives," *Carbon Capture Science & Technology* 11 (2024): 100191.
8. D. Li, S. Xie, J. Liang, et al., "Structure Regulated Cusn Alloy Catalyst for Selective Electrochemical CO₂-to-Formate Conversion at Higher Current Densities," *Separation and Purification Technology* 340 (2024): 126545.
9. Q. Li, G. Liao, N. Liu, et al., "Synergistic Dielectric Barrier Discharge Plasma in Binary Foam Metals for Enhanced CO₂ Conversion," *Journal of Physics D: Applied Physics* 58 (2025): 375205.
10. S. Li, Y. Wang, K. Zhang, et al., "Engineering In2O3 Catalysts Using Dielectric Barrier Discharge Plasma for Selective CO₂ Conversion to CO," *Journal of Alloys and Compounds* 1039 (2025): 183304.
11. A. K. Worku, D. W. Ayele, D. B. Deepak, A. Y. Gebreyohannes, S. D. Agegnehu, and M. L. Kolhe, "Recent Advances and Challenges of Hydrogen Production Technologies via Renewable Energy Sources," *Advanced Energy and Sustainability Research* 5 (2024): 2300273.
12. C. Wang, Z. Feng, Y. Zhao, et al., "Preparation and Properties of Ion Exchange Membranes for PEMFC With Sulfonic and Carboxylic Acid Groups Based on Polynorbornenes," *International Journal of Hydrogen Energy* 42 (2017): 29988–29994.
13. Z. Feng, G. Gupta, and M. Mamlouk, "A Review of Anion Exchange Membranes Prepared via Friedel-Crafts Reaction for Fuel Cell and Water Electrolysis," *International Journal of Hydrogen Energy* 48 (2023): 25830–25858.
14. Y. Luo, Y. Qiao, H. He, et al., "Rapid Synthesis of PtRu Nanoparticles on Aniline-Modified SWNTs in EMSI Engineering for Enhanced Alkaline Water Electrolysis," *Journal of Power Sources* 631 (2025): 236297.
15. S. Li, Z. Xin, Y. Luo, et al., "Enhancing Direct Borohydride Fuel Cell Performance via Low-Temperature Plasma Pretreatment of Cobalt Hydroxide Catalysts," *Ionics* 31 (2025): 4591–4602.
16. Z. Feng, G. Gupta, and M. Mamlouk, "Robust Poly(P-Phenylene Oxide) Anion Exchange Membranes Reinforced With Pore-Filling Technique for Water Electrolysis," *Journal of Applied Polymer Science* 141 (2024): e55340.
17. G. Liao, S. Li, Y. Luo, et al., "Plasma-Synthesized Ru-B Double Oxides Catalysts for Enhanced Fuel Cell Performance," *Journal of Alloys and Compounds* 1013 (2025): 178599.
18. H. S. Das, M. M. Rahman, S. Li, and C. W. Tan, "Electric Vehicles Standards, Charging Infrastructure, and Impact on Grid Integration: A Technological Review," *Renewable and Sustainable Energy Reviews* 120 (2020): 109618.
19. C. T. J. Roebroek, G. Duveiller, S. I. Seneviratne, E. L. Davin, and A. Cescatti, "Releasing Global Forests From Human Management: How Much More Carbon Could Be Stored?," *Science* 380 (2023): 749–753.
20. Z. Feng, P. O. Esteban, G. Gupta, D. A. Fulton, and M. Mamlouk, "Highly Conductive Partially Cross-Linked Poly(2,6-dimethyl-1,4-phenylene Oxide) as Anion Exchange Membrane and Ionomer for Water Electrolysis," *International Journal of Hydrogen Energy* 46 (2021): 37137–37151.
21. S. Zheng, Z. Feng, H. Che, W. Hao, Y. Hua, and Z. Gao, "Enhanced Stability of Quaternary Ammonium Cross-Linked SEBS Anion Exchange Membranes for Fuel Cells," *ChemistrySelect* 10 (2025): e202500481.
22. M. M. Hasan, R. Haque, M. I. Jahirul, et al., "Advancing Energy Storage: The Future Trajectory of Lithium-Ion Battery Technologies," *Journal of Energy Storage* 120 (2025): 116511.
23. N. Nasajpour-Esfahani, H. Garmestani, M. Bagheritabar, et al., "Comprehensive Review of Lithium-Ion Battery Materials and Development Challenges," *Renewable and Sustainable Energy Reviews* 203 (2024): 114783.
24. F. Zhan, L. Huang, Y. Luo, et al., "Recent Advances on Support Materials for Enhanced Pt-Based Catalysts: Applications in Oxygen Reduction Reactions for Electrochemical Energy Storage," *Journal of Materials Science* 60 (2025): 2199–2223.
25. M. Alkhedher, A. B. Al Tahhan, J. Yousaf, M. Ghazal, R. Shahbazian-Yassar, and M. Ramadan, "Electrochemical and Thermal Modeling of Lithium-Ion Batteries: A Review of Coupled Approaches for Improved Thermal Performance and Safety Lithium-Ion Batteries," *Journal of Energy Storage* 86 (2024): 111172.
26. L. Li, J. Yang, R. Tan, et al., "Large-Scale Current Collectors for Regulating Heat Transfer and Enhancing Battery Safety," *Nature Chemical Engineering* 1 (2024): 542–551.
27. C. Shi, Z. Li, M. Wang, et al., "Electrolyte Tailoring and Interfacial Engineering for Safe and High-Temperature Lithium-Ion Batteries," *Energy & Environmental Science* 18 (2025): 3248–3258.
28. M. Zhang, R. Tan, M. Wang, Z. Zhang, C. John Low, and Y. Lai, "Hypercrosslinked Porous and Coordination Polymer Materials for Electrolyte Membranes in Lithium-Metal Batteries," *Battery Energy* 3 (2024): 20230050.
29. Y. Luo, Y. Zhang, J. Zhu, et al., "Material Engineering Strategies for Efficient Hydrogen Evolution Reaction Catalysts," *Small Methods* 8 (2024): e2400158.
30. Z. Feng, G. Gupta, and M. Mamlouk, "Degradation of QPPO-Based Anion Polymer Electrolyte Membrane at Neutral Ph," *RSC Advances* 13 (2023): 20235–20242.

31. X. Li, Y. Zhao, Z. Feng, et al., "Ring-Opening Metathesis Polymerization for the Preparation of Polynorbornene-Based Proton Exchange Membranes With High Proton Conductivity," *Journal of Membrane Science* 528 (2017): 55–63.
32. K. Yang, L. Zhang, W. Wang, et al., "Multiscale Modeling for Enhanced Battery Health Analysis: Pathways to Longevity," *Carbon Neutralization* 3 (2024): 348–385.
33. F. Fasulo, A. Massaro, A. Pecoraro, A. B. Muñoz-García, and M. Pavone, "Role of Defect-Driven Surface Reconstructions in Transition Metal Oxide Electrocatalysis Towards OER/ORR: A Quantum-Mechanical Perspective," *Current Opinion in Electrochemistry* 42 (2023): 101412.
34. X. Liu, L. Zhang, H. Yu, et al., "Bridging Multiscale Characterization Technologies and Digital Modeling to Evaluate Lithium Battery Full Lifecycle," *Advanced Energy Materials* 12 (2022): 1.
35. G. Bao, X. Liu, B. Zou, et al., "Collaborative Framework of Transformer and LSTM for Enhanced State-of-Charge Estimation in Lithium-Ion Batteries," *Energy* 322 (2025): 135548.
36. B. Zou, M. Xiong, H. Wang, et al., "A Deep Learning Approach for State-of-Health Estimation of Lithium-Ion Batteries Based on a Multi-Feature and Attention Mechanism Collaboration," *Batteries* 9 (2023): 329.
37. N. Takenaka, A. Bouibes, Y. Yamada, M. Nagaoka, and A. Yamada, "Frontiers in Theoretical Analysis of Solid Electrolyte Interphase Formation Mechanism," *Advanced Materials* 33 (2021): 2100574.
38. Z. Shumin, G. Haitao, N. E. Svetlana, and W. Bao, "Air-Exposed Lithium Metal as a Highly Stable Anode for Low-Temperature Energy Storage Applications," *Energy Materials* 2 (2022): 200042.
39. X. Liu, K. Yang, B. Zou, et al., "Accurate Estimation of State of Health for Lithium-Ion Batteries Based on Pyraformer and TimeGAN Data Augmentation," *Journal of Power Sources* 640 (2025): 236722.
40. Z. Feng, I. Eiubovi, Y. Shao, Z. Fan, and R. Tan, "Review of Digital Twin Technology Applications in Hydrogen Energy," *Chain* 1 (2024): 54–74.
41. H. Lee, T. Kwak, W. Lee, J. Song, and D. Kim, "Effect of Surface Topography on Dendritic Growth in Lithium Metal Batteries," *Journal of Power Sources* 552 (2022): 232264.
42. C. Sun, X. Ji, S. Weng, et al., "50C Fast-Charge Li-Ion Batteries Using a Graphite Anode," *Advanced Materials* 34 (2022): 2206020.
43. H. Zhang, H. Liu, L. F. J. Piper, M. S. Whittingham, and G. Zhou, "Oxygen Loss in Layered Oxide Cathodes for Li-Ion Batteries: Mechanisms, Effects, and Mitigation," *Chemical Reviews* 122 (2022): 5641–5681.
44. Z. Feng, Y. Luo, D. Li, J. Pan, R. Tan, and Y. Chen, "Integrating Digital Twins and Machine Learning for Advanced Control in Green Hydrogen Production," *Chain* 2 (2025): 1–14.
45. L. Ma, Y. Xu, H. Zhang, F. Yang, X. Wang, and C. Li, "Co-Estimation of State of Charge and State of Health for Lithium-Ion Batteries Based on Fractional-Order Model With Multi-Innovations Unscented Kalman Filter Method," *Journal of Energy Storage* 52 (2022): 104904.
46. A. X. Mu, B. J. Zhang, C. G. Li, D. Z. Xiao, E. F. Zeng, and F. J. Liu, "Estimating SOC and SOH of Energy Storage Battery Pack Based on Voltage Inconsistency Using Reference-Difference Model and Dual Extended Kalman Filter," *Journal of Energy Storage* 81 (2024): 110221.
47. P. Reshma and J. Manohar, "Collaborative Evaluation of SOC, SOP and SOH of Lithium-Ion Battery in an Electric Bus Through Improved Remora Optimization Algorithm and Dual Adaptive Kalman Filtering Algorithm (Vol 68, 107573, 2023)," *Journal of Energy Storage* 79 (2024): 110112.
48. Z. Feng, J. Huang, S. Jin, G. Wang, and Y. Chen, "Artificial Intelligence-Based Multi-Objective Optimisation for Proton Exchange Membrane Fuel Cell: A Literature Review," *Journal of Power Sources* 520 (2022): 230808.
49. X. Han, M. Ouyang, L. Lu, J. Li, Y. Zheng, and Z. Li, "A Comparative Study of Commercial Lithium Ion Battery Cycle Life in Electrical Vehicle: Aging Mechanism Identification," *Journal of Power Sources* 251 (2014): 38–54.
50. J. Yang, W. Fang, J. Chen, and B. Yao, "A Lithium-Ion Battery Remaining Useful Life Prediction Method Based on Unscented Particle Filter and Optimal Combination Strategy," *Journal of Energy Storage* 55 (2022): 105648.
51. Z. Feng, S. Jin, H. Xiang, et al., "Artificial Intelligence-Based Optimization for Ring-Opening Metathesis Polymerization of Proton Exchange Membrane," *Journal of Polymer Research* 30 (2023): 418.
52. B. Ma, H.-Q. Yu, W.-T. Wang, et al., "State of Health and Remaining Useful Life Prediction for Lithium-Ion Batteries Based on Differential Thermal Voltammetry and a Long and Short Memory Neural Network," *Rare Metals* 42 (2023): 885–901.
53. J. Schmitt, I. Horstkötter, and B. Bäker, "Effective Estimation of Battery State-of-Health by Virtual Experiments via Transfer- and Meta-Learning," *Journal of Energy Storage* 63 (2023): 106969.
54. B. Jiang, J. Zhu, X. Wang, X. Wei, W. Shang, and H. Dai, "A Comparative Study of Different Features Extracted From Electrochemical Impedance Spectroscopy in State of Health Estimation for Lithium-Ion Batteries," *Applied Energy* 322 (2022): 119502.
55. X. Wang, J. Li, R. Wang, and Y. Wu, "Lithium Battery Digital Twin Model With Incremental Learning," *Chain* 1 (2024): 249–262.
56. X. Kang, F. Yang, Z. Zhang, et al., "A Corrosion-Resistant Rumoni Catalyst for Efficient and Long-Lasting Seawater Oxidation and Anion Exchange Membrane Electrolyzer," *Nature Communications* 14 (2023): 3607.
57. Y. Gao, K. Liu, C. Zhu, X. Zhang, and D. Zhang, "Co-Estimation of State-of-Charge and State-of-Health for Lithium-Ion Batteries Using an Enhanced Electrochemical Model," *IEEE Transactions on Industrial Electronics* 69 (2022): 2684–2696.
58. J. Shao, J. Li, W. Yuan, et al., "A Novel Method of Discharge Capacity Prediction Based on Simplified Electrochemical Model-Aging Mechanism for Lithium-Ion Batteries," *Journal of Energy Storage* 61 (2023): 106788.
59. X. Ye, X. Rui, X. Lei, D. Jun-Fan, and H. Jia-Qi, "Recent Advances in Anion-Derived Seis for Fast-Charging and Stable Lithium Batteries," *Energy Materials* 1 (2021): 100013.
60. Y.-G. Lv, G.-P. Zhang, Q.-W. Wang, and W.-X. Chu, "Thermal Management Technologies Used for High Heat Flux Automobiles and Aircraft: A Review," *Energies* 15 (2022): 8316.
61. S. Ma, M. Jiang, P. Tao, et al., "Temperature Effect and Thermal Impact in Lithium-Ion Batteries: A Review," *Progress in Natural Science: Materials International* 28 (2018): 653–666.
62. M. Waqas, S. Ali, C. Feng, D. Chen, J. Han, and W. He, "Recent Development in Separators for High-Temperature Lithium-Ion Batteries," *Small* 15 (2019): e1901689.
63. J. Jaguemont and F. Bardé, "A Critical Review of Lithium-Ion Battery Safety Testing and Standards," *Applied Thermal Engineering* 231 (2023): 121014.
64. T. Wickramanayake, M. Javadipour, and K. Mehran, "A Novel Solver for an Electrochemical–Thermal Ageing Model of a Lithium-Ion Battery," *Batteries* 10 (2024): 126.
65. F. Pistorio, D. Clerici, F. Mocera, and A. Somà, "Coupled Electrochemical–Mechanical Model for Fracture Analysis in Active Materials of Lithium Ion Batteries," *Journal of Power Sources* 580 (2023): 233378.

66. K. Yang, L. Zhang, Z. Zhang, et al., “Battery State of Health Estimate Strategies: From Data Analysis to End-Cloud Collaborative Framework,” *Batteries* 9 (2023): 351.
67. M. Bin Jassar, C. Michel, S. Abada, et al., “A Joint DFT-KMC Study To Model Ethylene Carbonate Decomposition Reactions: SEI Formation, Growth, and Capacity Loss During Calendar Aging of Li-Metal Batteries,” *ACS Applied Energy Materials* 6 (2023): 6934–6945.
68. E. W. C. Spotte-Smith, R. L. Kam, D. Barter, et al., “Toward a Mechanistic Model of Solid–Electrolyte Interphase Formation and Evolution in Lithium-Ion Batteries,” *ACS Energy Letters* 7 (2022): 1446–1453.
69. S.-H. Pan, S. Nachimuthu, B. J. Hwang, G. Brunklaus, and J.-C. Jiang, “Synergistic Dual Electrolyte Additives for Fluoride Rich Solid-Electrolyte Interface on Li Metal Anode Surface: Mechanistic Understanding of Electrolyte Decomposition,” *Journal of Colloid and Interface Science* 649 (2023): 804–814.
70. A. Lamorgese, R. Mauri, and B. Tellini, “Electrochemical-Thermal P2D Aging Model of a LiCoO₂/graphite Cell: Capacity Fade Simulations,” *Journal of Energy Storage* 20 (2018): 289–297.
71. S. Yang, Y. Hua, D. Qiao, Y. Lian, Y. Pan, and Y. He, “A Coupled Electrochemical-Thermal-Mechanical Degradation Modelling Approach for Lifetime Assessment of Lithium-Ion Batteries,” *Electrochimica Acta* 326 (2019): 134928.
72. N. Kamyab, J. W. Weidner, and R. E. White, “Mixed Mode Growth Model for the Solid Electrolyte Interface (SEI),” *ECS Meeting Abstracts* MA2019-01 (2019): 371.
73. J. M. Reniers, G. Mulder, and D. A. Howey, “Review and Performance Comparison of Mechanical-Chemical Degradation Models for Lithium-Ion Batteries,” *Journal of the Electrochemical Society* 166 (2019): A3189–A3200.
74. P. Barai, K. Smith, C.-F. Chen, G.-H. Kim, and P. P. Mukherjee, “Reduced Order Modeling of Mechanical Degradation Induced Performance Decay in Lithium-Ion Battery Porous Electrodes,” *Journal of the Electrochemical Society* 162 (2015): A1751–A1771.
75. X. Lin, J. Park, L. Liu, Y. Lee, A. M. Sastry, and W. Lu, “A Comprehensive Capacity Fade Model and Analysis for Li-Ion Batteries,” *Journal of the Electrochemical Society* 160 (2013): A1701–A1710.